







Temperature-controlled synthesis of hollow, porous gold nanoparticles with wide range light absorption

J. Depciuch^{1,*} , M. Stec² , A. Maximenko¹, J. Baran² , and M. Parlinska-Wojtan^{1,*} 

¹Institute of Nuclear Physics Polish Academy of Sciences, 31-342 Kraków, Poland

²Department of Clinical Immunology, Institute of Pediatrics, Jagiellonian University Medical College, 30-663 Kraków, Poland

Received: 26 November 2019

Accepted: 2 January 2020

Published online:

8 January 2020

© The Author(s) 2020

ABSTRACT

An easy synthesis method of hollow, porous gold nanoparticles (AuHP NPs) with controlled diameter and pores sizes and with a wide range of light absorbance (continuous between 500 and 900 nm) is presented together with the explanation of the nanoparticle formation mechanism. The NPs were investigated using transmission electron microscopy (TEM) combined with the selected area electron diffraction patterns, X-ray diffraction and ultraviolet–visible spectroscopy. TEM images showed that changing the synthesis temperature allows to obtain AuHP NPs with sizes from 35 ± 4 nm at 60 °C to 76 ± 8 nm at 90 °C. The effects of nanoscale porosity on the far- and near-field optical properties of the nanoparticles, as well as on effective conversion of electromagnetic energy into thermal energy, were applied in simulated photothermal cancer therapy. The latter one was simulated by irradiation of two cancer cell lines SW480 and SW620 with lasers operating at 650 nm and 808 nm wavelengths. The mortality of cells after using the synthesized AuHP NPs as photosensitizers is between 20 and 50% and increases with the decrease in the diameter of the AuHP NPs. All these attractive properties of the AuHP NPs make them find application in many biomedical studies.

Introduction

Gold nanoparticles (Au NPs) are characterized by plasmonic optical properties [1–3], which can be manipulated by changing their geometry [4]. Therefore, literature describes Au NPs having shapes such as: spherical, nanorods [5], nanoprisms [6, 7], nanoshells [8] and nanocages [9], leading to different

optical properties. The possibility to change the absorption spectral range by Au NPs made these nanoparticles find potential applications in optoelectronics [10], photonics [11], spectroscopy [12, 13] as well as biomedical fields, especially in photothermal anticancer therapy (PTT), where Au NPs are used as photosensitizers [14]. However, the Au NPs applied in the PTT should absorb light with wavelength higher than 650 nm [15]. Hollow, porous gold

Address correspondence to E-mail: joanna.depciuch@ifj.edu.pl; magdalena.parlinska@ifj.edu.pl

nanoparticles show a wide spectral range of the absorbed light [16]. Indeed, this kind of porous, hollow nanostructures are characterized by three-dimensional nanoscale networks, which are very important in the effective absorption of light. This is due to the fact that conversion of the electromagnetic energy into thermal energy is higher in porous than in solid nanostructures [16].

Nowadays, the main methods to obtain hollow, porous gold nanoparticles are: sacrificial template [17], self-assembly [18], and electrochemical methods [19], dealloying [20–22] or galvanic replacement [23]. However, in these methods, atoms of other elements have to be used in the synthesis protocols making the final gold hollow, porous nanoparticles consist of atoms of gold and other elements, leading to worse plasmonic properties. Moreover, the nanoparticles obtained from the template synthesis methods are larger than 100 nm, and their structure is very often not hollow. These structures look like spheres, which are coated with an incomplete layer of the second element [17], and this effect is similar for porous spherical nanoparticles. Self-assembly [18] and electrochemical methods [19] lead to the formation of porous, but aggregated nanoparticles. Currently, the most popular synthesis methods of nanoporous gold nanoparticles are concentrated on the dealloying approach. The core regions of nanoparticles synthesized by dealloying are solid. The biggest obstacle in obtaining porous and hollow Au NPs using this method is the very large dispersive force among Au atoms [23]. However, porous Au NPs were successfully synthesized in several papers [19, 23, 24]. Unfortunately, the synthesis time of these nanoparticles is very long and requires high-temperature alloying and harsh dealloying processes [23]. Moreover, the sizes of the synthesized Au NPs are larger than 150 nm [24]. Furthermore, galvanic replacement process allows to obtain porous and hollow nanoparticles, but these NPs are composed from more than one element. Sun and Xia showed the synthesis of gold nanocages using galvanic replacement methods [23]. In their paper, they not only presented hollow porous gold nanoshells (nanocages), but they also described the mechanism of the formation these NPs, which has two steps. Moreover, they showed that using this method, it is possible to control the surface plasmon resonance (SPR) peaks positions, which is very important for the photothermal properties of NPs [23]. Silva et al.

showed the galvanic replacement reaction controlled by temperature, which leads to obtain trimetallic compositions of nanoparticles. Moreover, they emphasize that only combined galvanic replacement with co-reduction reactions controlled by temperature allows obtaining nanostructures with shapes, which do not represent the hollow analogues of the starting template nanocrystals [20]. Furthermore, Erlebacher et al. obtained nanoporous gold sheets; however, the percentage of gold atoms in the sheet was only 32%, while silver atoms constituted 68% [25]. Moreover, the obtained nanostructures were agglomerated, which generally suffers from slow energy transfer from the electromagnetic wave to the nanoparticles [25].

Herein, we present a fast synthesis of hollow, porous gold nanoparticles (AuHP NPs) with temperature-controlled size of the pores. Our method employs quick nucleation and growth of Au NPs and the stability conditions of cetyltrimethylammonium bromide (CTAB). The obtained Au NPs have pores and a hollow structure, very wide spectral range of the absorbed light and strong plasmon resonance. Furthermore, the hollow and porous Au NPs are characterized by very effective conversion of the electromagnetic energy to thermal energy, which can make them applicable in photothermal therapy of cancer. In the present study, the morphology of the obtained AuHP NPs is systematically characterized and a detailed formation mechanism of the nanoparticles is provided.

Materials and methods

Materials

Cetrimonium bromide (CTAB), gold(III) chloride hydrate (HAuCl_4), silver nitrate (AgNO_3), sodium borohydride (NaBH_4), ascorbic acid ($\text{C}_6\text{H}_8\text{O}_6$) and all other chemicals were ordered from Sigma–Aldrich.

Synthesis of porous gold nanoparticles

To prepare solution I, the CTAB solutions was prepared as follows: 0.364 g of CTAB was dissolved in the 5 mL of H_2O . Next, 0.0017 g of HAuCl_4 was dissolved in the 10 mL of H_2O . In the second step, to the CTAB solution 5 mL of HAuCl_4 solution was added and mixed under vigorous stirring. When the

solution was dissolved, 0.6 mL of 100×10^{-3} M NaBH_4 was added. Color of solution changed to red. Solution II was prepared as follows: 0.364 g of CTAB was dissolved in the 5 mL of H_2O . Then, 0.2 mL of 3.97×10^{-3} M AgNO_3 , 5 mL of 5×10^{-4} M HAuCl_4 , 140 μL of 7.9×10^{-2} M $\text{C}_6\text{H}_8\text{O}_6$ and 30 μL of solution I were added to the CTAB solutions and mixed under vigorous stirring in 60 °C, 70 °C, 80 °C and 90 °C, respectively.

TEM characterization

The morphology of the synthesized nanoparticles was examined by scanning transmission electron microscopy (STEM) using the high-angle annular dark-field detector (HAADF), in conventional and high-resolution modes. Selected area electron diffraction (SAED) patterns were taken in the TEM mode. All these measurements were performed on an aberration-corrected FEI Titan electron microscope operating at 300 kV equipped with a FEG cathode. The particle size distribution was evaluated based on the HRSTEM images taken from different areas of the TEM grids. For each sample, the diameter of 100 nanoparticles was measured.

X-ray diffraction

The global structure of obtained AuHP NPs was investigated by X-ray diffraction (XRD) analysis using a two-circle laboratory diffractometer Panalytical X'Pert Pro with $\text{Cu K}\alpha$ X-ray source ($\lambda\text{K}\alpha_1 = 1.5406 \text{ \AA}$) operated at 40 kV and 30 mA. For sample preparation, a concentrated particle suspension was deposited on a zero background holder, which was placed on a sample spinner. The data in the range 30–85° (2θ) were collected in Bragg–Brentano geometry at room temperature. The patterns were analyzed using Rietveld refinement through the Fullprof program, where a modified Thompson-Cox-Hastings pseudo-Voigt function was used as a profile function, and the background was fitted by 6-coefficient polynomial function.

UV–Vis spectroscopy

UV–Vis spectra were obtained using Lambda Bio20 spectrometer (Perkin Elmer). The measurements were done using 240 nm/min speed of scan and

1 nm spectral resolution. The spectral range was from 200 to 900 nm.

Cell culture

Colon cancer cell lines (SW480, SW620) were obtained due to courtesy of Prof. Caroline Dive, Paterson Institute for Cancer Research, University of Manchester. These cell lines were cultured in DMEM with high glucose (Corning, NY, USA) in a 37 °C humidified atmosphere with 5% CO_2 . All media were supplemented with 10% fetal bovine serum (FBS, Biowest, Nuaille, France) and gentamicin (50 $\mu\text{g}/\text{ml}$), (PAN-Biotech, Aidenbach, Germany). The cells were cultured by bi-weekly passages and regularly were tested for *Mycoplasma* sp. contamination by PCR-ELISA kit (Roche, Mannheim, Germany) according to the manufacturers' instruction.

MTS assay

Cytotoxic activity of AuF NPs against human colon cancer cells (SW480 and SW620) was determined by using 3-(4,5-dimethylthiazol-2-yl)-5-(3-carboxymethoxyphenyl)-2-(4-sulfophenyl)-2H-tetrazolium (MTS) assay (CellTiter 96® AQueous One Solution Cell Proliferation Assay, Promega, Madison, WI). Briefly, cells were cultured in flat-bottom 96-well plates (Sarstedt, Numbrecht, Germany) at a density $1 \times 10^4/\text{well}$ in DMEM medium containing 10% FBS. After 24 h, the 20 μL of $3, 88 \times 10^{-3}$ mg/ml Au NPs solutions was added to the cells. After additional 24 h of culture, 20 μL of MTS (CellTiter 96® AQueous One Solution Cell Proliferation Assay, Promega) dye solution was added per well and incubated for 2 h. The quantity of formazan product, directly proportional to the number of living cells in culture, was detected by absorbance measurement at 490 nm with a 96-well plate reader (Spark® Tecan, Mannedorf, Switzerland).

Photothermal conversion efficiency determined from the time constant

To determine the photothermal conversion efficiency of AuP1–AuP4 NPs, the solutions of nanoparticles were placed into a glass cuvette and irradiated with low-intensity LED lasers with two different, 650 and 808 nm, wavelengths. A digital multimeter connected to a small Pt-100 thermo-resistor located inside of the

cuvette was used to measure the temperature evolution during irradiation.

Light source and cells irradiation protocols

The irradiation of SW480 and SW620 colon cancer cells cultured with AuP1–AuP4 NPs was done using low-intensity 650 nm and 808 nm LED lasers during 5 min. The intensity of the LED lasers was 100 mW/cm².

Statistical analysis

The results obtained from MTS assay are represented as the means ± SEM (the standard error of the mean) with the *T* test. *P* value < 0.05 was considered to be statistically significant.

Results and discussion

Scanning transmission electron microscopy (STEM) images of synthesized AuHP NPs, Fig. 1a1, b2–d2, showed that the obtained nanoparticles have a spherical shape; however, the surface of the AuHP NPs is porous. As we can see in Fig. 1, the size of the obtained AuHP NPs, as well as the size of the pores, can be systematically controlled by temperature. With increasing temperature, the size of the AuHP NPs increases, while the size of the pores decreases. The AuHP NPs synthesized at 60 °C have an average size of 35 ± 4 nm (Fig. 1d1), while the AuHP NPs synthesized at 70 °C, 80 °C and 90 °C have sizes of 44 ± 5 nm, 50 ± 7 nm and 76 ± 8 nm, respectively (Fig. 1d2–d4). Therefore, we will refer these particles as AuHP1 NPs, AuHP2 NPs, AuHP3 NPs and AuHP4 NPs. The following numbers mean the increasing size of the obtained nanoparticles resulting from different synthesis temperatures. The reason for the formation of AuHP NPs with different diameters and pore sizes will be discussed in detail in the mechanism section.

We acquired selected area electron diffraction (SAED) patterns from the four analyzed nanoparticle samples, Fig. 1a3–d3, which showed that all synthesized nanoparticles are crystalline. Moreover, the SAED showed that the randomly oriented AuHP NPs crystallites could be indexed with the lattice parameter of gold [24]. Although all SAED patterns consisted of rings, we observed differences in the

respective patterns, originating from the increasing size of the AuHP NPs. Indeed, the SAED pattern taken from the AuHP1 NPs sample is composed from rather blurred rings, which is expected due to the smallest size (35 nm) of the NPs, Fig. 1a3. As expected, the rings in the SAED patterns of AuHP2 NPs (Fig. 1b3) become sharper and contain more and more spots, which is related to the increasing average size of the nanoparticles. Similarly, the SAED patterns of AuHP3 NPs, Fig. 1c3, are composed of even sharper rings and contain even more spots than sample AuHP2 NPs; however, the sharpest spots are visible in the SAED pattern of the largest AuHP4 NPs, Fig. 1d3. To resolve the global structure of obtained AuHP NPs, X-ray diffraction (XRD) was employed, Fig. 2.

X-ray diffraction showed that the peaks from the experimental patterns for all AuHP NPs match well with the (111), (200), (220), (311) and (222) diffraction peaks of the standard of gold [26] (Fig. 2) and a good refinement of the patterns was made using the gold fcc phase. The ratios of the (200) and (220) peak intensities to the (111) peak intensity for all Au NPs coincide well with the bulk intensity ratios ($I_{200}/I_{111} \approx 0.52$ and $I_{220}/I_{111} \approx 0.32^{26}$), which may indicate that the nanoparticles were composed of various facets. There was no preferential direction of the nanoparticles growth, and this tendency did not depend on the reaction temperature [27]. The average coherent scattering length ($\langle D \rangle$) of the four investigated nanoparticle samples, which we assumed to be equal to crystallite sizes, was around $\langle D_{Au} \rangle \approx 12$ nm and did not significantly change with reaction temperature. Comparing the crystallite sizes with the sizes of nanoparticles obtained from TEM measurements, it may be deduced that the size of the nanoparticles increased with the reaction temperature due to agglomeration of a larger number of small monocrystalline gold seeds with a size of around 12 nm. Moreover, this assumption could be confirmed by the absence of size dependence of the lattice parameter, which was observed for gold nanoparticles [28, 29]. It was found that the lattice parameter of the fabricated nanoparticles did not depend on the reaction temperature and had the same value ($a = 4.077(1)$ Å) for the four investigated nanoparticle samples. Thereby, the synthesized AuHP NPs can be described as agglomerations of Au 12 nm monocrystals, where the number of monocrystals in these agglomerations increases with

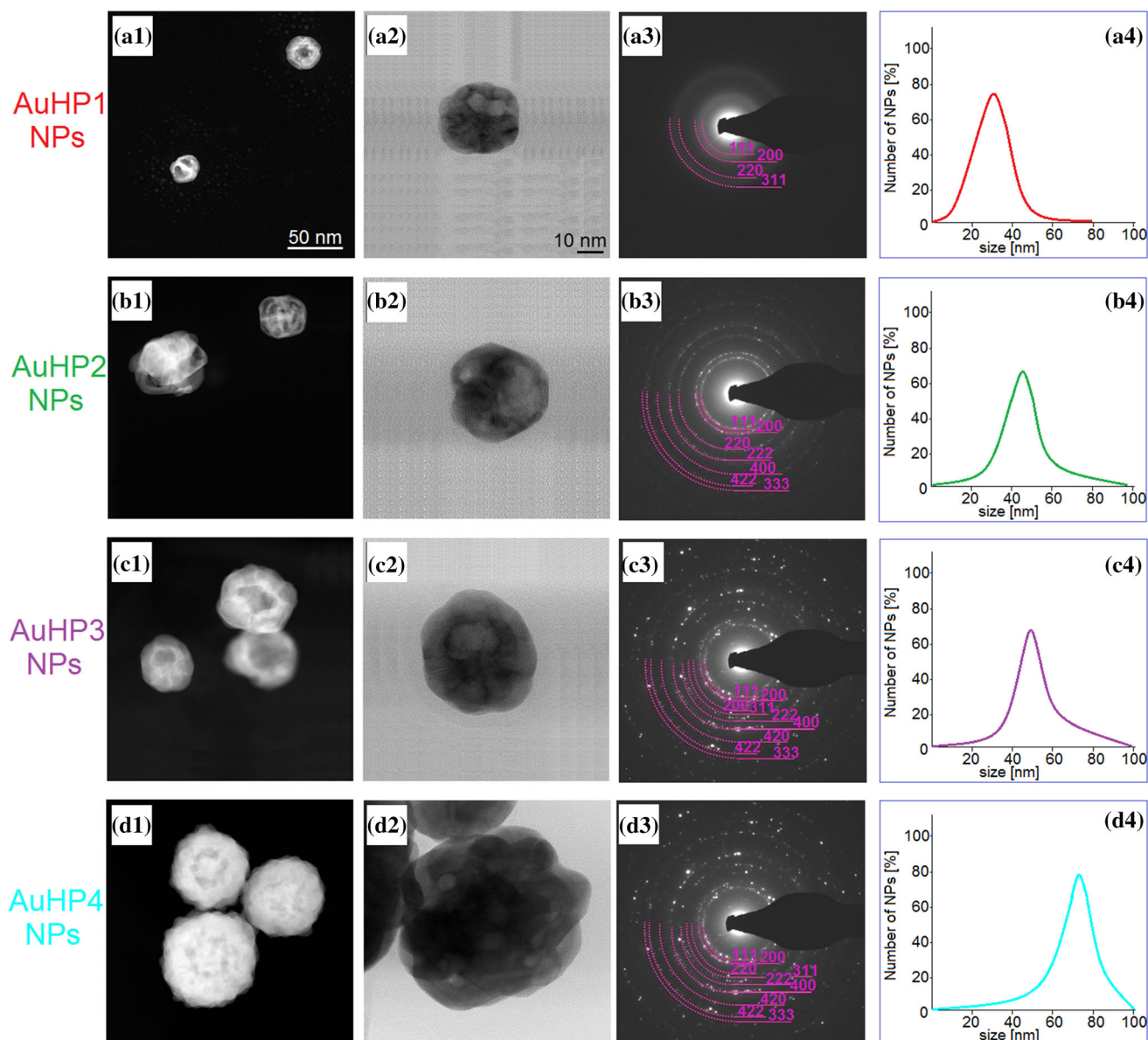


Figure 1 STEM HAADF overview images (a1–d1) and STEM BF magnified images (a2–d2) with corresponding diffraction patterns (a3–d3) and average sizes (a4–d4) of: AuHP1 NPs (a1–

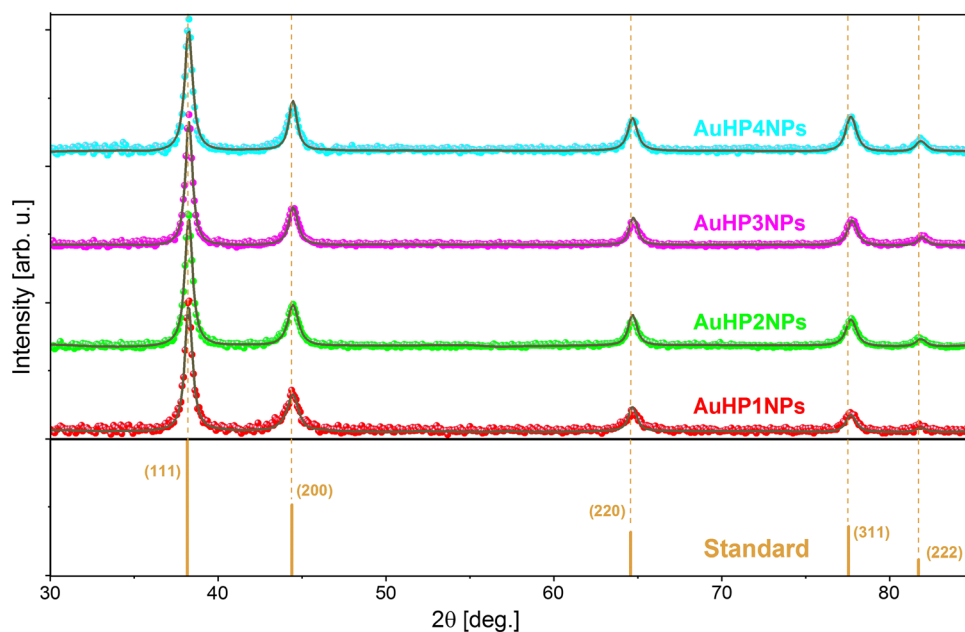
a4); AuHP2 NPs (b1–b4); AuHP3 NPs (c1–c4); AuHP4 NPs (d1–d4). The scales are the same for the images in each column.

the reaction temperature, and thus, the nanoporous particles grow in size.

To better understand the synthesis mechanism of AuHP NPs with different sizes and pores, a control experiment was done. In this experiment, we synthesized nanoparticles at room temperature; therefore, the speed of the synthesis was slower (Supplementary material, Figure S1). The shape of the obtained nanoparticles was rather rod-like, and they did not exhibit porosity. The presence of the CTAB molecules and AgBr formed from AgNO_3

blocks the growth of nanoparticles in the {110} direction, thus allowing growth along the {001} planes causing the shape of nanoparticles to be rod-like [30] as visible in Figure S1. An increase of the synthesis temperature caused that the speed of the AuCl_4^- reduction was faster, and consequently, the number of nucleation sites favoring the formation of pores [31] increased. In parallel, the increase of temperature leads to destabilization of the CTAB and AgBr molecules, causing the shape of the nanoparticles to be spherical rather than rod-like. The

Figure 2 X-ray diffraction patterns of nanoparticles synthesized at different temperatures compared to standard reference of gold [26]. For the experimental patterns, closed circles present experimental data and solid black lines corresponds to calculated Rietveld refinement plots.



proposed mechanism of synthesis of porous Au NPs suggests that their formation results from the temperature-controlled increase of the gold precursor reduction speed and unblocking of the nanoparticles growth in the {110} direction by destabilization of CTAB and AgBr molecules. Additionally, the Au seeds present in the solution combine with the already formed AuHP NPs contributing to their growth, which is nicely visualized in the TEM image in Fig. 3. The scheme of the proposed growth mechanism of porous AuHP NPs with different sizes is also presented in Fig. 3. Moreover, the proposed mechanism can be confirmed by comparing the nanoparticles grown at room temperature with the ones grown at 60 °C, as the latter ones seem to be “swollen” due to the formation of pores. From the literature it is known that, at higher temperatures, the optimal system energy has higher values than at lower temperatures [32], while the lowest system energy exhibit small, spherical nanoparticles. Therefore, when the synthesis temperature increases leading to the formation of bigger AuHP NPs, their pores become smaller to lower system energy [33].

The ultraviolet–visible (UV–Vis) spectra, presented in Fig. 4, showed that the position of localized plasmon resonances of the AuHP NPs depends on the size of the nanoparticles. Moreover, the synthesized AuHP NPs showed a very wide range of light absorption, which is continuous between 500 and 900 nm. We noticed that smaller AuHP1 and AuHP2

NPs absorb more light, compared to larger AuHP3 and AuHP4 NPs. However, these two larger nanoparticles absorb light in a wider range than the smaller ones. Zhang et al. showed that the nanoscale porosity creates sharp, nanoscale surface features, which are responsible for the increase of intense near-field “hot spots” upon plasmonic excitation [16]. Moreover, they showed that the intensity of the optical properties of the nanoparticles increased with the porosity of the Au NPs surface. The large width of the AuHP NPs SPR peaks caused these nanoparticles to be applied in many fields of industry and medicine, because they can absorb light in wavelengths from 500 to 900 nm or even more. Therefore, we investigated the thermal properties of our AuHP NPs by changing the temperature of the nanoparticles by laser irradiation. For this purpose, two low-intensity 100 mW/cm² LED lasers with two different wavelengths (650 and 808 nm) were used. The temperature changes were observed during 5 min by a digital multimeter connected to a small Pt-100 thermo-resistor located inside of the nanoparticle solutions. In comparison with the control water solution, the increases of temperature in AuHP1–AuHP4 NPs solutions were observed for both wavelengths: 650 nm and 808 nm. Looking at the temperature rise, higher values for all nanoparticles solutions were observed for the 650 nm laser than for the 808 nm one. For the 650 nm laser, we measured a temperature increase of approximately 9 °C being

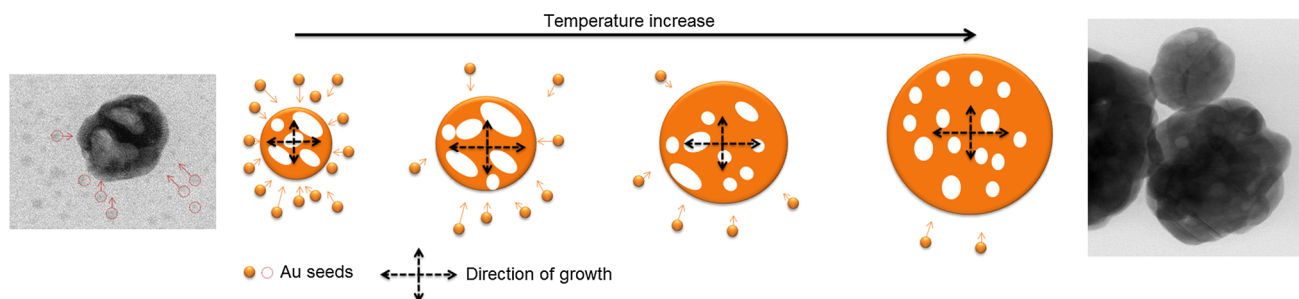


Figure 3 Scheme of the mechanism of AuHP NPs formation with controlled sizes of nanoparticles and pores. The scheme is not in scale.

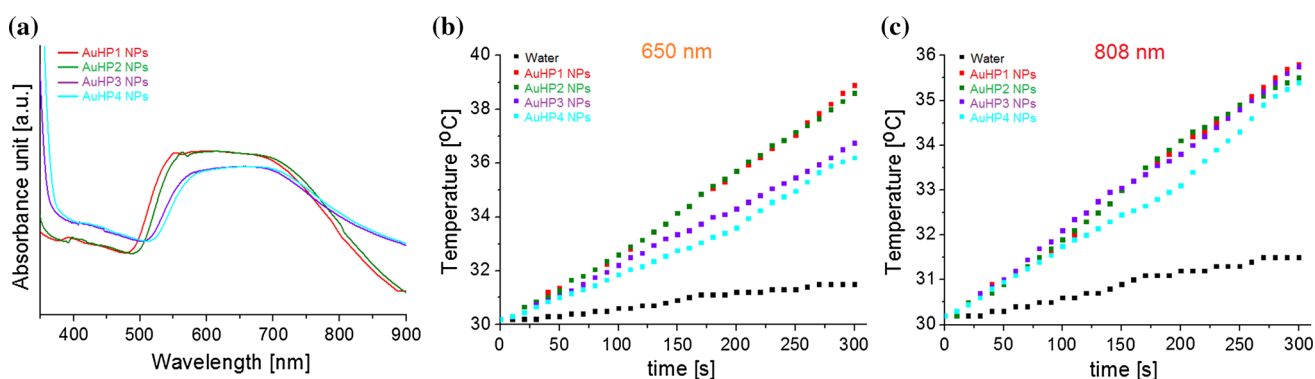


Figure 4 Surface plasmon absorption of the synthesized AuHP NPs (a); temperature changes in AuHP1 NPs (red circles); AuHP2 NPs (green triangles); AuHP3 NPs (violet stars), AuHP4 NPs

(aqua diamonds) solutions irradiated by 650 nm (b), 808 nm (c) lasers. Black color corresponds to the water (control) solution.

similar for AuHP1 and AuHP2 NPs, while for larger nanoparticles this increase was around ~ 7 °C. In the case of the 808 nm laser, a higher temperature increase was observed for the AuHP3 and AuHP4 NPs. This observation is explained by the larger size of these nanoparticles compared to AuHP1 and AuHP2 NPs and by the presence of smaller pores. As observed in the obtained UV–Vis spectra, larger nanoparticles showed light absorbance in the range near to red light, while the smaller NPs showed light absorbance at lower wavelengths [23]. Moreover, finite difference time-domain (FDTD) simulations by other authors, showed that the calculated near-field distributions ($|E/E_0|^2$) for the spherical non-porous and spherical porous Au NPs with the same sizes is around ten times higher for porous nanoparticles [16]. Moreover, nanoparticles with pores have larger numbers of hot spots with local field enhancements, compared to bulk spherical Au NPs. These calculations also showed that the highest near-field distribution was present around the border of pores and nanoparticles, which means that with the increase of the pores and decrease of the NPs size, the optical

properties of NPs are better. The high values of the near-field distributions for the smaller NPs indicate a high conversion of the electromagnetic energy into thermal energy, which is shown in Fig. 4b and c.

We also investigated the possibility of using the nanoparticles as photosensitizers in the PTT of cancer. For this purpose, we cultured cells with AuHP1–AuHP4 NPs, and subsequently we irradiated these cells by 650 nm and 808 nm lasers during 5 min. We used this time because after that period, differences in the viability of cells were not observed (Supplementary materials, Figure S2). For evaluating the effectiveness of the PTT simulated by laser irradiation in the presence of AuHP NPs, MTS assays were done, Fig. 5. These tests showed that the viability of cancer cells cultured only with the AuHP NPs depends on the size of the nanoparticles. For the smallest AuHP1 NPs with the largest pores, the viability of cells was two times smaller than for the larger AuHP4 NPs in both cell lines. Interestingly, using the AuHP NPs as photosensitizers caused very significant increase of the percentage of death cells. In both tested cell lines, higher mortality was observed

for irradiation by the 650 nm laser. Moreover, also for the irradiated cells, the mortality increased with the decrease of the AuHP NPs size. For the SW480 cell line irradiated by the 650 laser, the mortality of cells varied from 50% for AuHP1 NPs to 70% for AuHP4 NPs, while for the SW620 cell line, the viability of irradiated cells cultured with nanoparticles was from 60% for the smallest AuHP NPs to 75% for the largest obtained NPs. Irradiation of cells by light with 808 nm wavelength caused mortality of 45% SW480 cells for small AuHP NPs and 23% for large AuHP

NPs, while for the other cell line, the mortality was between 42 and 20% and it decreased with the increase of the size of the hollow porous gold nanoparticles. The differences in the mortality between the cells were caused by the type of investigated cell lines [34]. In our case, we tested cells from the primary tumor (SW480) and from a metastatic lesion to the lymph node (SW620). The metastatic lesion cells are very often more aggressive than cells from the primary tumor [35]. Therefore, in our study we observed lower effectiveness of the mortality of

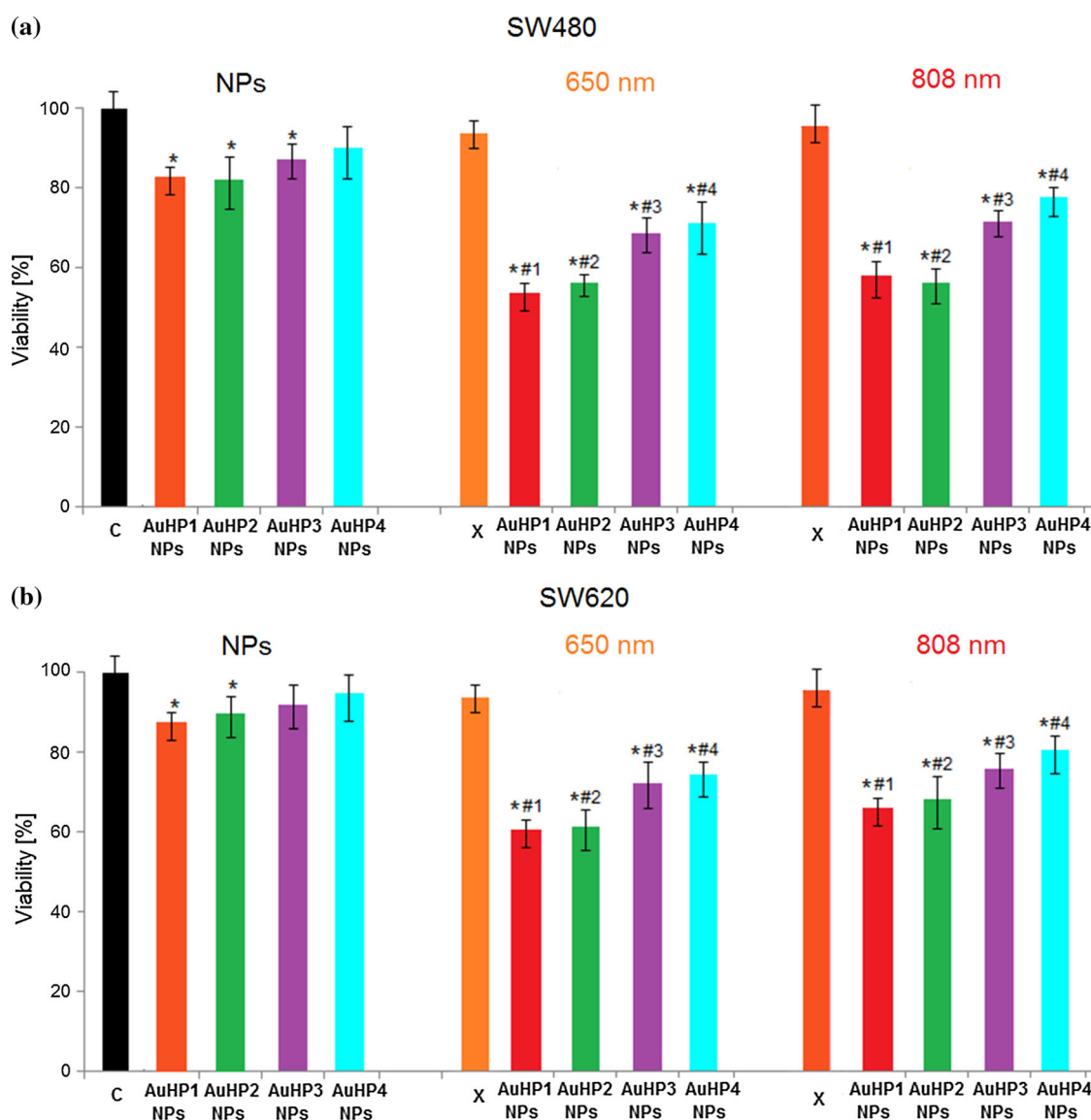


Figure 5 Viability of colon cancer SW480 (a) and SW620 (b) cell lines: after addition of AuHP1–AuHP4 NPs, without irradiation as well as irradiated by 650 nm and 808 nm lasers. Data were considered as significant when $*p < 0.05$ versus Control;

$\#p < 0.05$ versus AuHP1–AuHP4 NPs, respectively. “X” corresponds to the cell line cultured without AuHP NPs and irradiated for 5 min.

SW620 cells cultured with AuHP NPs and irradiated by lasers, than in the case of SW480 cells. Moreover, the high mortality of the irradiated and non-irradiated cells cultured with the smallest AuHP NPs was caused by their large active surface, provided by the presence of large pores. Thus, porous NPs are more toxic than spherical nanoparticles [36, 37]. It is correlated with the large number of active places, which could interact with cancer cells, generating free radicals and oxidative stress [38, 39]. These kinds of surfaces are also responsible for the optical and photodynamic properties of nanoparticles [40]. In the case of hollow porous gold nanoparticles, the small size of AuHP1 NPs and large size of pores causes the value of the local electromagnetic field, which is responsible for the values of NPs photothermal efficiency, to be the highest.

Summarizing, we developed a synthesis method of hollow porous gold nanoparticles, where the size of the NPs and well as the one of the pores can be controlled by changing the synthesis temperature: from 35 ± 4 nm at 60 °C to 76 ± 8 nm at 90 °C. The formation of the hollow porous gold nanoparticles was studied in detail using TEM with SAED and XRD patterns. Owing to their porosity, the obtained AuHP NPs showed wide range light absorption and high conversion of the electromagnetic energy into thermal energy. These properties were applied to simulate the photothermal cancer therapy (PTT). With all of these attractive characteristics combined together and the possibility of controlling the growth of hollow, porous Au NPs, our synthesis method and the obtained AuHP NPs are expected to generate a strong impact on many biomedical applications, especially *in vitro* and *in vivo* applications. Moreover, the hollow, porous structures have very large number of active places and active surfaces; therefore, these structures can find potential application not only in anticancer therapy, but also in catalysis, offering more effective catalysts than the commercially available ones [41]. Furthermore, in comparison with bulk nanoparticles, hollow NPs have refractive index sensitivity [42]. Thanks to this, AuHP NPs can find application in biosensing, e.g., very small DNA molecules [43]. Moreover, AuHP NPs can effectively enhance the specific absorption of photoacoustic signal, which allow to use nanoparticles not only in photothermal anticancer therapy, but also as photoacoustic contrast agents [44].

Acknowledgements

The authors thank the Institute of Engineering Materials and Biomaterials of the Silesian University of Technology for the use of the Titan FEI TEM instrument. Partial financial support by Pik-Instruments is greatly acknowledged.

Author contributions

JD synthesized AuHP NPs, measured UV–Vis spectra, and temperature increase in AuHP NPs solutions; MP-W performed TEM and SAED measurements; AM performed XRD measurements; MS cultured the cell lines and made MTS assay. The manuscript was written through contributions of all authors.

Compliance with ethical standards

Conflict of interest The authors declare no competing financial interest.

Electronic supplementary material: The online version of this article (<https://doi.org/10.1007/s10853-020-04345-8>) contains supplementary material, which is available to authorized users.

Open Access This article is licensed under a Creative Commons Attribution 4.0 International License, which permits use, sharing, adaptation, distribution and reproduction in any medium or format, as long as you give appropriate credit to the original author(s) and the source, provide a link to the Creative Commons licence, and indicate if changes were made. The images or other third party material in this article are included in the article's Creative Commons licence, unless indicated otherwise in a credit line to the material. If material is not included in the article's Creative Commons licence and your intended use is not permitted by statutory regulation or exceeds the permitted use, you will need to obtain permission directly from the copyright holder. To view a copy of this licence, visit <http://creativecommons.org/licenses/by/4.0/>.

References

- [1] Halas NJ, Lal S, Chang WS, Link S, Nordlander P (2011) Plasmons in strongly coupled metallic nanostructures. *Chem Rev* 111(6):3913–3961
- [2] Murphy CJ, Sau TK, Gole AM, Orendorff CJ, Gao J, Gou L, Hunyadi SE, Li T (2005) Anisotropic metal nanoparticles: synthesis, assembly, and optical applications. *J Phys Chem B* 109(29):13857–13870
- [3] Jain PK, Huang X, El-Sayed IH, El-Sayed MA (2008) Noble metals on the nanoscale: optical and photothermal properties and some applications in imaging, sensing, biology and medicine. *Acc Chem Res* 41(12):1578–1586
- [4] Xia Y, Halas NJ (2005) Shape-controlled synthesis and surface plasmonic properties of metallic nanostructures. *MRS Bull* 30(5):338–348
- [5] Nikoobakht B, El-Sayed MA (2003) Preparation and growth mechanism of gold nanorods (NRs) using seed-mediated growth method. *Chem Mater* 15(10):1957–1962
- [6] Jin R, Cao YW, Mirkin CA, Kelly KL, Schatz GC, Zheng JG (2001) Photoinduced conversion of silver nanospheres to nanoprisms. *Science* 294(5548):1901–1903
- [7] Santos I, Marzan LM (2002) Synthesis of silver nanoprisms in DMF. *Nano Lett* 2(8):903–905
- [8] Halas N (2005) Playing with plasmons: tuning the optical resonant properties of nanoshells. *MRS Bull* 30(5):362–367
- [9] Chen J, Wiley B, Li ZY, Campbell D, Saeki F, Cang H, Au L, Lee J, Li X, Xia Y (2005) Gold nanocages: engineering their structure for biomedical applications. *Adv Mater* 17(18):2255–2261
- [10] Knight MW, Sobhani H, Nordlander P, Halas NJ (2011) Photodetection with active optical antennas. *Science* 332(6030):702–704
- [11] Oulton RF, Sorger VJ, Zentgraf T, Ma RM, Gladden C, Dai L, Bartal G, Zhang X (2009) Plasmon lasers at deep sub-wavelength scale. *Nature* 461(7264):629–632
- [12] Willets KA, Van Duyne RP (2007) Localized surface plasmon resonance spectroscopy and sensing. *Annu Rev Phys Chem* 58:267–297
- [13] Camden JP, Dieringer JA, Zhao J, Van Duyne RP (2008) Controlled plasmonic nanostructures for surface-enhanced spectroscopy and sensing. *Acc Chem Res* 41(12):1653–1661
- [14] Giljohann DA, Seferos DS, Daniel WL, Massich MD, Patel PC, Mirkin CA (2010) Gold nanoparticles for biology and medicine. *Angew Chem Int Ed Engl* 49(19):3280–3294
- [15] Riley DS, Day ES (2017) Gold nanoparticle-mediated photothermal therapy: applications and opportunities for multimodal cancer treatment. *Wiley Interdiscip Rev Nanomed Nanobiotechnol* 9(4):16. <https://doi.org/10.1002/wnan.1449>
- [16] Zhang Q, Large N, Nordlander P, Wang H (2014) Porous Au nanoparticles with tunable plasmon resonance intense field enhancements for single-particle SERS. *J Phys Chem Lett* 5(2):370–374
- [17] Nyce GW, Hayes JR, Hamza AV, Satcher JH (2007) Synthesis and characterization of hierarchical porous gold materials. *Chem Mater* 19(3):344–346
- [18] Kim M, Jeong GH, Lee KY, Kwon K, Han SW (2008) Fabrication of nanoporous superstructures through hierarchical self-assembly of nanoparticles. *J Mater Chem* 18:2208–2212
- [19] Nishio K, Masuda H (2011) Anodization of gold in oxalate solution to form a nanoporous black film. *Angew Chem Int Ed Engl* 50(7):1603–1607
- [20] da Silva AGM, Rodrigues TS, Haigh SJ, Camargo PHC (2017) Galvanic replacement reaction: recent developments for engineering metal nanostructures towards catalytic applications. *Chem Commun* 53:7135–7148
- [21] Ding Y, Erlebacher J (2003) Nanoporous metals with controlled multimodal pore size distribution. *J Am Chem Soc* 125(26):7772–7773
- [22] Huang JF, Sun IW (2005) Fabrication and surface functionalization of nanoporous gold by electrochemical alloying/dealloying of Au–Zn in an ionic liquid, and the self-assembly of L-cysteine monolayers. *Adv Funct Mater* 15(6):989–994
- [23] Sun Y, Xia Y (2003) Alloying and dealloying processes involved in the preparation of metal nanoshells through a galvanic replacement reaction. *Nano Lett* 3(11):1569–1572
- [24] Pedireddy S, Lee HK, Tjiu WW, Phang IY, Tan HR, Chua SQ, Troadec C, Ling XY (2014) One-step synthesis of zero-dimensional hollow nanoporous gold nanoparticles with enhanced methanol electrooxidation performance. *Nature Commun* 5(4947):9
- [25] Erlebacher J, Aziz MJ, Karma A, Dimitroy N, Sieradzki K (2001) Evolution of nanoporosity in dealloying. *Nature* 410:450–453
- [26] Swanson H, Tatge E (1953) Standard X-ray diffraction powder patterns. United States Department of Commerce, Washington
- [27] Kwon K, Lee KY, Lee YW, Kim M, Heo J, Ahn SJ, Han SW (2007) Controlled synthesis of icosahedral gold nanoparticles and their surface-enhanced Raman scattering property. *J Phys Chem C* 111(3):1161–1165
- [28] Leontyev IN, Kuriganova AB, Leontyev NG, Hennem L, Rakhmatullin A, Smirnova NV, Dmitriev V (2019) *RSC Adv* 9:31196–31201
- [29] Vermaak JS, Kuhlmann-Wilsdorf D (1968) Measurement of the average surface stress of gold as a function of

- temperature in the temperature range 50–985. deg. *J Phys Chem* 72(12):4150–4154
- [30] Liu M, Sionnest P (2005) Mechanism of silver(I)-assisted growth of gold nanorods and bipyramids. *J Phys Chem B* 109(47):22192–22200
- [31] Hu J, Jiang R, Zhang H, Guo J, Wang J (2018) Colloidal porous gold nanoparticles. *Nanoscale* 10:18473–18481
- [32] Kozlov SM, Kovacs G, Ferrando R, Neyman KM (2015) How to determine accurate chemical ordering in several nanometer large bimetallic crystallites from electronic structure calculations. *Chem Sci* 6:3868–3880
- [33] Vollath D, Fischer FD, Holec D (2018) Surface energy of nanoparticles—influence of particle size and structure. *Beilstein J Nanotechnol* 9:2265–2276
- [34] Sonavage G, Tomoda K, Makino K (2008) In vitro permeation of gold nanoparticles through rat skin and rat intestine: effect of particle size. *Colloids Surf B Biointerfaces* 66(2):274–280
- [35] Leibovitz A, Stinson JC, McCombs WB, McCoy CE, Mazur KC, Mabry ND (1976) Classification of human colorectal adenocarcinoma cell lines. *Cancer Res* 36(12):4562–4569
- [36] Sun YN, Wang CD, Zhang XM, Ren L, Tian XH (2011) Shape dependence of gold nanoparticles on in vivo acute toxicological effects and biodistribution. *J Nanosci Nanotechnol* 11(2):1210–1216
- [37] Kah JCY, Grabinski C, Untener E, Garrett C, Chen J, Zhu D, Hussain SM, Schifferli K (2014) Protein coronas on gold nanorods passivated with amphiphilic ligands affect cytotoxicity and cellular response to penicillin/streptomycin. *ACS Nano* 8(5):4608–4620
- [38] Schins RP (2002) Mechanisms of genotoxicity of particles and fibers. *Inhal Toxicol* 14(1):57–78
- [39] Vallyathan V, Shi X (1997) The role of oxygen free radicals in occupational and environmental lung diseases. *Environ Health Prospect* 105(1):165–177
- [40] Wang X, Li G, Ding Y, Sun S (2014) Understanding the photothermal effect of gold nanostars and nanorods for biomedical applications. *RSC Adv* 4:30375–30383
- [41] Cui QL, Xia BH, Mitzscherling S (2015) Preparation of gold nanostars and their study in selective catalytic reactions. *Colloids Surf A* 465:20–25
- [42] Zhang JZ, Noguez C (2008) Plasmonic optical properties and applications of metal nanostructures. *Plasmonics* 3(4):127–150
- [43] Liu SF, Liu J, Han XP, Cui YN, Wang W (2010) Electrochemical DNA biosensor fabrication with hollow gold nanospheres modified electrode and its enhancement in DNA immobilization and hybridization. *Biosens Bioelectron* 25(7):1640–1645
- [44] Lu W, Huang Q, Ku G (2010) Photoacoustic imaging of living mouse brain vasculature using hollow gold nanospheres. *Biomaterials* 31(9):2617–2626

Publisher's Note Springer Nature remains neutral with regard to jurisdictional claims in published maps and institutional affiliations.